Feature Article

Aspects of Electrohydrodynamic Instabilities at Polymer Interfaces

Thomas P. Russell*, Zhiqun Lin, Erik Schäffer[1], and Ullrich Steiner[2]

Department of Polymer Science and Engineering, University of Massachusetts, Amherst
[1]Fakultaet Fuer Physik, Universitaet Konstanz, Germany
[2]Department of Polymer Chemistry, University of Groningen, The Netherlands
(Received December 10, 2002; Accepted January 15, 2003)

Abstract: Electrospinning is emerging as a simple means of producing fibers with diameters ranging from 0.02 μm to many microns. Electrospinning, however, relies on the force generated by an electric field on the surface of a polymer solution to either enhance instabilities in a thinning jet or to rapidly elongate a jet of polymer solution form a nozzle. In this article, the fundamental physics and fluid dynamics on the subject matter are described, and some of the relevant parameters in electrodynamic instabilities at polymer interfaces are discussed in some detail.

Keywords: Electrohydrodynamic, Instabilities, Surfaces, Interfaces

Electrospinning is emerging as a simple means of producing fibers with diameters ranging from 0.02 μm to many microns[1-4]. Electrospinning, however, relies on the force generated by an electric field on the surface of a polymer solution to either enhance instabilities in a thinning jet or to rapidly elongate a jet of polymer solution form a nozzle. While electrospinning is only now gaining in popularity, the fundamental physics and fluid dynamics have been understood from some time[5-11]. It seems appropriate, at this time, therefore, to discuss some of the relevant parameters of importance in electrohydrodynamic instabilities and to point to some other areas of fundamental science and applications that are seeing a growth. In our laboratories we have been particularly interested in electrohydrodynamic instabilities in thin polymer films and we use our studies to highlight some of the salient features.

It is well known that there is thermally excited capillary wave at the interface, where the amplitude and wavelength are governed by the interfacial tension and any pressures acting on the interface. An external electric field applied across the interface exerts an electrostatic pressure on the interface that will amplify the fluctuations. The electrostatic pressure works against interfacial tension, which is given by the product of the interfacial energy and the interface area, to generate electrohydrodynamic instabilities. The small wavelength fluctuations are suppressed since they are too costly energetically. The long wavelength fluctuations, on the other hand, are also suppressed due to the fluid dynamics. This leads to the fastest growth of one wavelength, which is amplified, and eventually bridges between two electrodes. Electrohydrodynamic instabilities forms the basis for the electrospinning process where an electric potential is placed across the interface of a solution emerging from the tip of an orifice and the ground where the spun fibers are collected. Here, we review and analyze experiments that address the

---

*Corresponding author: mrsec@polysci.umass.edu

fundamental physics underlying electrospinning by focusing on the simplest cases of pure polymer/air and polymer/polymer interfaces. Figure 1 shows the general sample configuration in our studies. The indium-tin-oxide coated (ITO) microscope slides served as the upper electrode. It is transparent and good for real time optical microscopy observations. The separation distance between Si substrate and ITO glass can be controlled by evaporating thin rails of SiO_x on the top of ITO glass or Si substrate as an insulating spacer. In the case of single layer film and bilayer studies, the medium 1 and the medium 2 are air/liquid, and liquid 1/liquid 2, respectively.

A simple linear stability analysis indicated that the instability exhibits a well-defined lateral wavelength that follows a power-law dependence on the applied electric field, in agreement with theory[12,13]. We extend this theoretical model in terms of characteristic wavelength at liquid/air interface to more general case for liquid/liquid bilayer and obtain experimental data to test the model. The characteristic wavelength at the interface of liquid/liquid bilayer can be given as[14,15]

$$\lambda = \frac{2\pi}{U\left|\dfrac{1}{\varepsilon_2} - \dfrac{1}{\varepsilon_1}\right|}\left(\frac{\gamma_{12}}{\varepsilon_0}\right)^{1/2}\left(\frac{d-h_0}{\varepsilon_1} + \frac{h_0}{\varepsilon_2}\right)^{3/2} \qquad (1)$$

where d-h and h are the film thicknesses of liquid 1 and liquid 2 with dielectric constants ε_1 and ε_2, respectively. γ_{12} is the interfacial tension between liquid 1 and 2, and ε_0 is the dielectric permittivity in vacuum.

The central finding in liquid/liquid bilayer study is a reduction of the length scale of dynamical instabilities induced by an electric field when the air/liquid interface is replaced by a liquid/liquid interface. A typical example is shown in Figure 2. In the first set of experiments, a layer of 140 nm polyisoprene, with an air gap of 940 nm with 20 V applied across the electrodes. An amplification of fluctuations at the PI/air interface occurred, leading to the creation of an
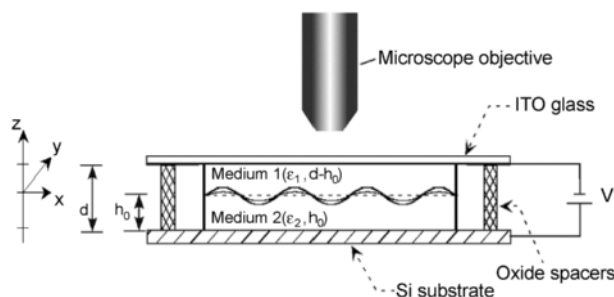
Figure 1. Sketch of the sample geometry used in the experiments. A bilayer of two liquids with film thickness of h_0 and $d-h_0$, respectively, is confined between two solid electrodes: a highly polished silicon wafer (lower electrode) and an ITO coated microscope slide (upper electrode). The distance between the two electrodes is controlled by the height of spacer structures (SiO_X) evaporated at the edges of the slides on top of the ITO. The temporal evolution of the confined samples under an applied electric field is studied by optical microscopy in the reflectance mode.
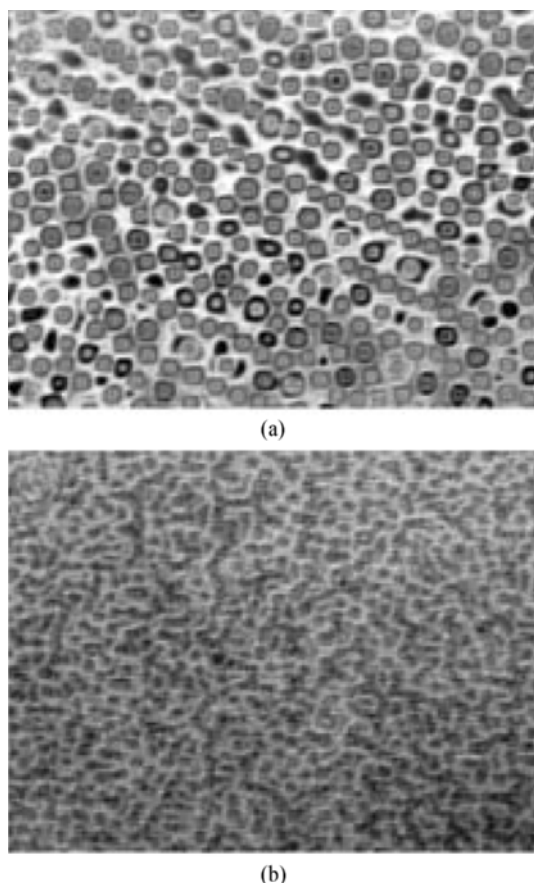

Figure 2. (a) Optical microscopy image of a thin liquid film of polyisoprene, (b) Optical microscopy image of a bilayer of polyisoprene and oligomeric dimethylsiloxane annealed for 2 days in an electric field ($d-h = 940$ nm, $h = 140$ nm, $V = 20$ V). In both figures the original color images were converted to gray scale. The dimensions of the images are 528 μm by 692 μm (taken from Ref. 14).

array of vertically standing PI columns (Figure 2(a)). The average distance between the center of two neighboring columns is $<d_{cyl-cyl}> = 47.4 \pm 4.4\ \mu$m. The influence of changes in ε and γ of the upper layer on the time and size scales of the evolving structures was investigated in the second set of experiments. Figure 2(b) shows the final state of a PI/polydimethyl-siloxane, PDMS bilayer annealed at ambient conditions. A visual comparison of Figures 2(a) and (b) shows a clear reduction in length scale, associated with the replacement of air by PDMS. The cylinder structures now exhibit a typical spacing of $<d_{cyl-cyl}> = 20.6 \pm 1.3\ \mu$m. This

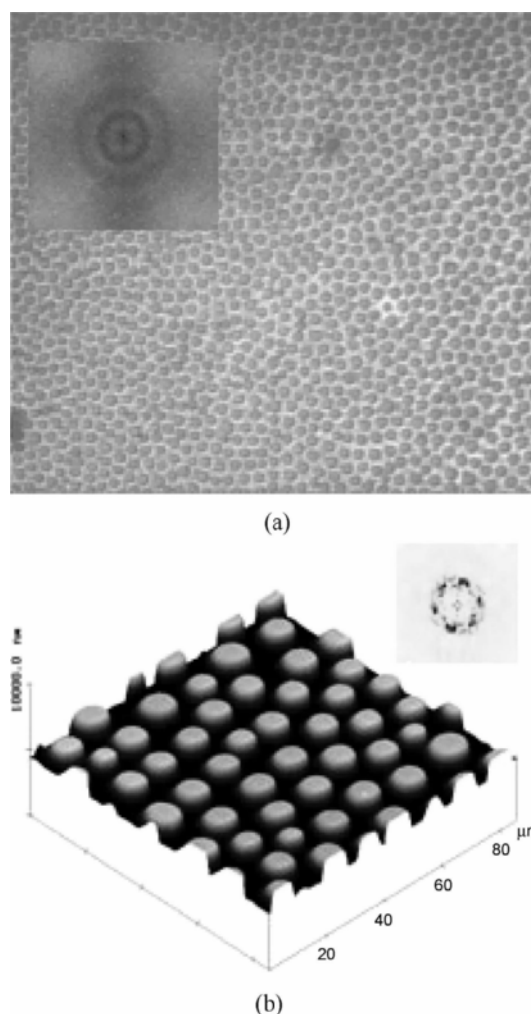**Figure 3.** (a) Optical micrograph of a PS ($h_{PS} = 550$ nm)/PDMS ($h_{PDMS} = 700$ nm) bilayer exposed to 50 V at 170 °C for one day. The image size is 438×398 μm². The original color images were auto leveled and contrasted, and then converted to a grayscale to enhance the weak contrast due to the small refractive index difference between PS and PDMS. The inset shows the 2D fast Fourier transform (FFT) pattern of the corresponding optical micrographs. (b) The 3D AFM height image of the PS/PDMS bilayer after removal of the upper PDMS layer with heptane. The 2D FFT of the AFM image is shown in the inset (taken from Ref. 15).

spacing is about one-half that observed in the single film experiments[14].

A systematic characterization of structure formation at the interface of the liquid/liquid bilayers in the electric field was also performed. Regardless of the polymers used, very good agreement over many orders of magnitude in reduced wavelength and field strength is observed using no adjustable parameters. An optical micrograph of the PS/PDMS bilayer after one day under a 50 V is shown in Figure 3(a). Columns of PS through the upper PDMS layer are evident in the micrograph. The formation of the cylindrical structures at the interface is clearly seen. A 2D Fast Fourier Transform (FFT) of the optical micrograph is shown in the inset. The appearance of a ring in the transform indicates that there is a well-defined center-to-center distance between adjacent PS columns of 13.0 μm. After removing the upper PDMS layer with heptane, AFM was used to examine the surface of the underlying PS layer, i.e., the interface between the PDMS and PS layers. Shown in Figure 3(b) is the AFM image of the PS surface obtained in the height mode. As seen, columns of PS have been produced by the electrostatic pressure acting on the original PDMS/PS interface. The average size of the columns is 8.5 ± 0.3 μm with an average center-to-center distance between adjacent PS columns of 13.0 ± 1.0 μm. Shown in the inset is a 2D fast Fourier Transform (FFT) of the AFM image. The six spots evident in these data indicate that, locally, there is a hexagonal symmetry in the lateral arrangement of the columns. Substituting the relevant parameters for the PDMS/PS bilayer case into equation (1) yields a characteristic distance of 15.8 μm, which agrees well with the 12.9 μm value measured experimentally[15].

In a second set of experiments, the upper PDMS layer was replaced by a PMMA layer to form PS/PMMA bilayer. Since the interfacial tension between PS and PMMA ($\gamma_{PS/PMMA}$ = 1.1 mN/m at 170 ^{o}C) is smaller than that for a PS/PDMS bilayer, ($\gamma_{PS/PDMS}$ = 6.1 mN/m) at any given temperature, then, from equation (1), it would be expected that the characteristic wavelength λ would decrease. Shown in Figure 4(a) is the optical micrograph of the PS/PMMA bilayer after one day at 170 ^{o}C with 30 V applied after selectively removing the upper PMMA layer. Direct images of the bilayer without removal of the upper layer were not easily seen, since the refractive indices of PS and PMMA, 1.591 and 1.49, respectively, are very similar. The 2D FFT shown in the inset exhibits a ring, indicative of a well-defined separation distance between the features at the interfaces. Analysis of the optical micrograph yields an average center-to-center distance between adjacent features of 4.0 ± 0.7 μm with an average diameter of the columns of 1.7 ± 0.3 μm. Shown in Figure 4(b) is an AFM height image after removal of the PMMA layer by rinsing with acetic acid. Rather than columns, however, the AFM image shows that the features are holes penetrating through the PS film. This results, primarily, from the thickness of the individual layers. Here,
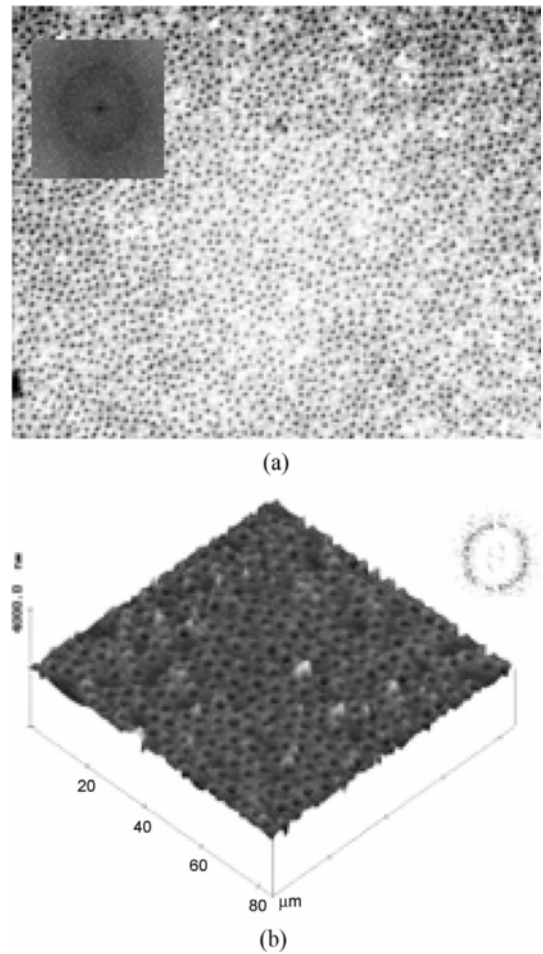

(a)

(b)

Figure 4. (a) An optical microscope image of PS/PMMA bilayer after removing the upper PMMA layer with acetic acid. The bilayer system held under 30 V at 170 ^{o}C for one day. The image size is 266×199 mm^2. The initial film thickness of PS and PMMA were 730 and 290 nm, respectively. The inset shows the 2D fast Fourier transform (FFT) pattern of the corresponding optical micrographs. (b) An AFM height image of the bilayer after removal of the upper PMMA layer. The 2D FFT of the AFM image is shown in the inset (taken from Ref. 15).

the underlying PS layer was much thicker than the PMMA overlayer. Consequently, in this case, PMMA columns form within the PS layer. From equation (1) λ = 2.8 μm which is in good agreement with the value determined experimentally[13].

The characteristic wavelength, λ, of fluctuations at the interface that are amplified by the applied electric field depends upon the sample geometry, the applied field and the dielectric constants of the materials. These parameters are explicitly shown in equation (1). We can define a reference wavelength and electric field as follows:

$$\lambda_0 = \frac{\varepsilon_0 U^2 (\varepsilon_1 - \varepsilon_2)^2}{\gamma_{12}(\varepsilon_1 \varepsilon_2)^{1/2}} \qquad (2)$$

and $E_0 = \dfrac{U}{\lambda_0}$ $\qquad\qquad$ (3)

Using these we can define a reduced wavelength and field by dividing λ and E by λ_0 and E_0, respectively. For the reduced wavelength we have:

$$\frac{\lambda}{\lambda_0} = 2\pi\left(\frac{E_1 E_2}{E_0^2}\right)^{-3/4} \qquad\qquad (4)$$

where E_1 and E_2 are the electric field strengths in layer 1 and 2, respectively. By replacing ε_1 with 1.0, E_2 with E_P, the dimensionless variables, can be reduced to the polymer thin film case investigated by Schäffer *et al.*[15].

A master curve where the reduced wavelength λ/λ_0 is plotted as a function of the reduced field strength $E_1 E_2/E_0^2$ is shown in Figure 5. Shown are experimental data obtained from different experiments where the geometry of the system, the field strengths and the polymers have been varied. In addition, data from previous experiments on single polymer layers are included. The solid line in the figure is the theoretical reduced wavelength as a function of the
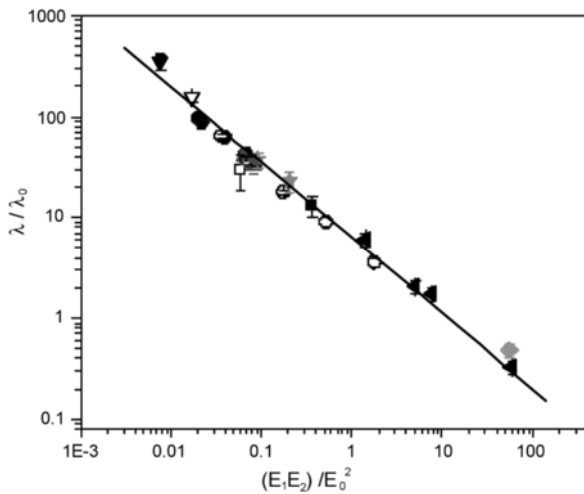

Figure 5. The master curve of the typical distance λ in varieties of thin film and bilayer experiments as a function of the electric field strength in the layer 1 and layer 2. The different symbols corresponded to ten data sets: ◆ PS/PMMA bilayer with h_{PS} = 730 nm, (d-h_{PS})$_{PMMA}$ = 290 nm, U = 30 V; ▼ PMMA/PDMS bilayer with h_{PMMA} = 180-290 nm, (d-h_{PMMA})$_{PDMS}$ = 690-1030 nm, U = 19-50 V; ★ PS/PDMS bilayer with h_{PS} = 305 nm, (d-h_{PS})$_{PDMS}$ = 400 nm and 720 nm respectively, U = 50 V; ▲ PS/PDMS bilayer with h_{PS} = 550 nm, (d-h_{PS})$_{PDMS}$ = 570 nm and 700 nm respectively, U = 50 V; O PSBr/air single layer with h_{PSBr} = 740 nm, d = 1.66-1.98 μm, U = 20-60 V; ● dPS/air single layer with h_{dPS} = 530 nm, d = 1.06-1.85 μm, U = 30 V, ▽, ▽, ■, and □ were the measurements from reference 3, which corresponded to PI/air thin film, PI/ODMS bilayer, OS/air thin film and OS/ODMS bilayer systems respectively. The straight line was calculated based on the equation (4) with a slope of −3/4 (taken from Ref. 15).

reduced field strength using no adjustable parameters. As can be seen, there is excellent agreement between experiment and theory over four orders of magnitude in the reduced wavelength and reduced field strength[15].

The derivation of equation (1) uses a linear approximation in treating the amplitude of fluctuations at the interface. Consequently, equation (1) should only be valid at the early stages of fluctuation growth and not, necessarily, at the latter stages of the process which includes the results shown here. Shown in Figure 6 are a series of AFM height images characterizing the development of structure at the interface of a PMMA/PDMS bilayer with 19 V applied at 170 °C at different times. Each of the images was obtained on different bilayer samples where the upper PDMS layer was removed with heptane. Figure 6(a) shows that the initial interface was featureless. With time, fluctuations having a well-defined lateral wavelength are seen to emerge (Figure 6(b)). The 2D FFT of this image, shown in the inset, exhibits a maximum characteristic of a wavelength or average center-to-center distance of 10.5 μm. As time progresses, the amplitude of the fluctuations increases, the fluctuations become sharper and well-defined and begin to show a lateral order, and instabilities that give rise to the formation of columns appear (Figure 6(c)). The 2D FFT of this AFM image, shown in the inset, exhibits a maximum corresponding to an average center-to-center distance of 10.5 μm, the same spacing seen at earlier times. The surface of the PMMA after the formation of PMMA columns that extend to the upper electrode is shown in Figure 6(d). Contact with the upper electrode is evidenced by the flattened top of the columns and a well-defined lateral ordering is evident. The 2D FFT shown in the inset exhibits a maximum corresponding to a cent-to-center distance between adjacent columns of 10.5 μm, the same as that seen at earlier times. The preservation of the characteristic distance throughout the growth of the columns justifies the comparison of the results obtained at later times to the linearized theoretical predictions. However, this does not hold true for the characteristic times describing the kinetic growth of these structures. As discussed earlier, discrepancies between the predicted times and those observed, based on the late stages of growth, are seen due to our inability to characterize the kinetics of the growth quantitatively[14]. These studies are currently in progress using fluorescent confocal microscopy.

The quantitative agreement between experiment and theoretical predictions in the master curve of Figure 5 shows that by controlling the sample geometry, the applied field or the interfacial energy, the size scale of the fluctuations can be controlled or manipulated. For a given geometry, polymer pair and field strength, reducing the interfacial tension provides a route to decrease the size scale of the fluctuations. Smaller size scale fluctuations that produce a larger interfacial area, can be amplified if the interfacial tension is reduced. It is well known that the addition of block copolymers that
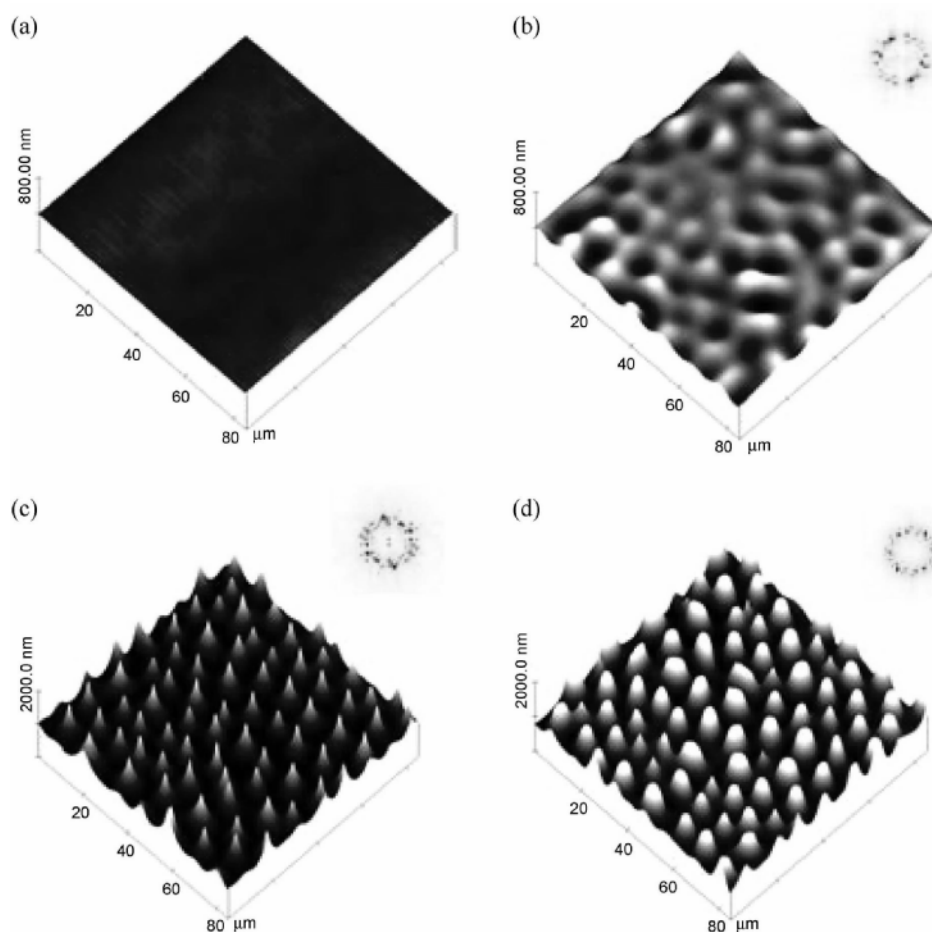
Figure 6. A series of AFM height images as a function of time of a PMMA/PDMS bilayer after removal of the PDMS layer (h_{PMMA} = 220 nm, h_{PDMS} = 890 nm) with 19 V applied with heptane. The insets show a FFT of the images. The time sequence of the images correspond to the (a) initial interface, (b) initial stages of fluctuation growth, (c) amplification of fluctuations, and (d) the impingement of PMMA columns on the upper electrode (taken from Ref. 15).

segregate to the to polymer/polymer interfaces reduces the interfacial tension and, hence, provides an easy route towards structures that are hundreds to tens of nanometers in size. In the case of thin polymer films, a surface-active agent should cause a similar effect. With fixed interfacial energies, increasing the electric field provides the easiest route to control the lateral length scales of the fluctuations. By combining both these effects, the characteristic lateral length scale of the fluctuations can easily be placed in the nanoscopic level. Studies are in progress to systematically vary the concentration of the copolymer at the interface so as to develop a protocol for controlling the lateral dimensions quantitatively.

External electric fields were also used to amplify interfacial fluctuations in the air/liquid 1/liquid 2 system where one polymer dewets the other[16]. Two different hydrodynamic regimes were found as a function of electric field strength. If heterogeneous nucleation leads to the formation of holes before the electrostatically driven instability sets in, the dewetting kinetics is not influenced by the electric field. Stronger electric fields lead to a spinodal electrohydrodynamic instability which causes the formation of polymer columns on top of the second polymer. The rapid column formation leads to a substantial deformation of the lower polymer layer at the column contact line, caused by the high viscous stress concentration there.

The sample setup of the air /PS/PMMA trilayer is shown in Figure 7. Rather than carrying out a time series with a constant applied field (which limits us to an optical investigation of the sample only), the use of a wedge geometry is an alternative means of observing (in a quasi static manner) the growth of the instability, since the onset of the instability scales with the sixth power of the electric field in the polymer film[13]. Several different instabilities of the liquid 1 layer can be observed on the same sample[16]: (1). For very large electrode spacings, the double film was predominately stable, except for isolated dewetting holes.
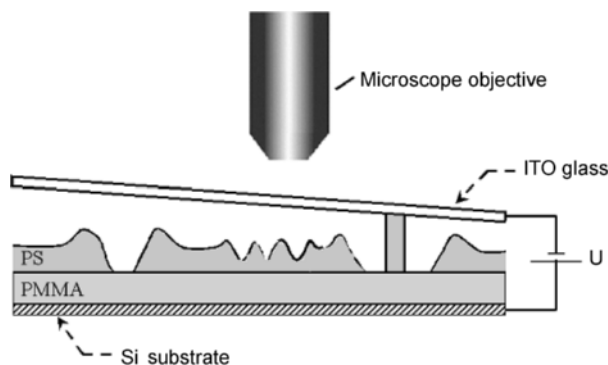
Figure 7. Typical sample configuration in the study. The air/ Polystyrene(PS)/Poly(methyl methacrylate) (PMMA) system was sandwiched between a highly polished and doped silicon wafer (lower electrode) and an ITO microscope slide (upper electrode). The distance between the two electrodes was controlled by evaporating SiO_x as a spacer (at the edges of the slides on top of the ITO). Typically, the electrode spacing varied by a few micrometers over a lateral distance of approx. 1 cm. The structure formations of the system under an applied electric field (0 V, 30 V, and 60 V) were studied by optical microscopy in the reflectance mode. After removal of the top electrode, the sample was imaged by atomic force microscopy (taken from Ref. 16).
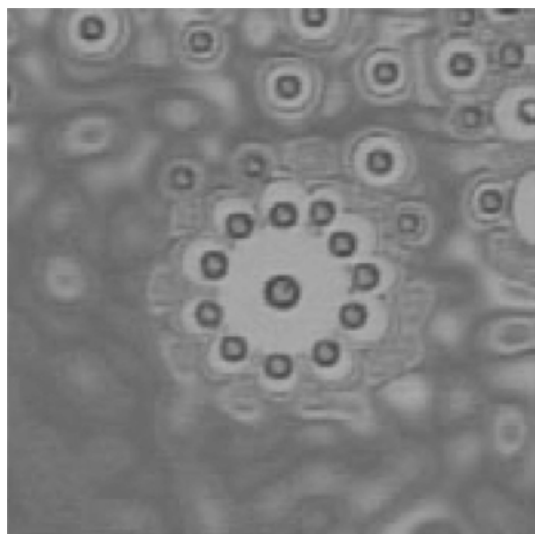

Figure 8. An optical microscope image of air/PS-96 k/PMMA-95 k trilayer with 30 V applied in the configuration shown in Figure 7. The image size was 212×212 mm^2 (taken from Ref. 16).

(2). For intermediate electrode spacings, an undulating instability of the liquid 1 surface with a characteristic wavelength is observed (see Figure 8, bottom left). (3). At small enough electrode spacings, an electrohydrodynamic instability caused the formation of liquid columns. This instability is accompanied by the dewetting of PS on top of PMMA. Both, the nucleated and spinodal instabilities are
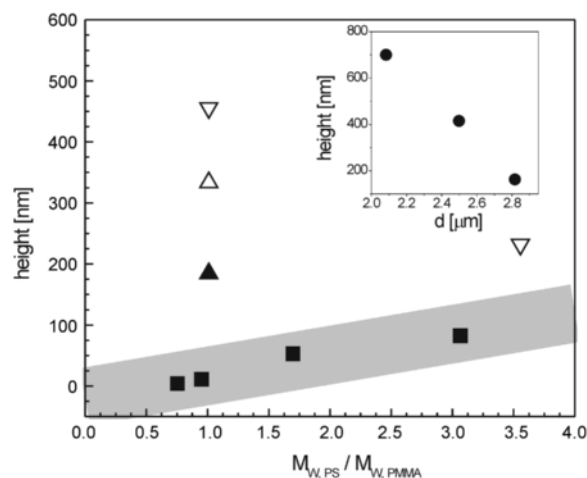

Figure 9. Deformation of height under the dewetting rim as a function of the ratio of the molecular weights of the PS and PMMA from Lambooy *et al*.[17] (black squares) and our experiments (gray area). The triangles are the deformations observed for the PMMA-95 k/PS-96 k system with 30 V applied (▲ : sample 2, △: sample 4) and the inverted triangles were obtained with 60 V applied for PMMA-95 k/PS-96 k (sample 3) and PMMA-27 k/PS-96 k (sample 9). The inset shows the deformation of height as a function of separation distance of the electrodes, *d*, for the PMMA-95 k/PS-96 k bilayer at 60 V applied field (samples 5, 6, 7) (taken from Ref. 17).

observed (see Figure 8 center and top right, respectively). The structure in the center of the micrograph consists of an initial column (primary cylinder) that was heterogeneously nucleated earlier in the experiment. As the dewetting rim grew in size and height, fluctuations with a characteristic spacing were amplified and grew into regularly spaced columns (secondary cylinders). Each secondary column was then surrounded by its own dewetting zone. As PS dewets the PMMA, PS accumulates in the dewetting rim, changing the position of the PS/air interface locally. This creates an instability along the rim which, in turn leads to the formation of secondary cylinders. Similar to the nucleated instability, the columns formed by a spinodal process (Figure 8 top right) are each surrounded by a dewetting zone.

The extent of the deformation of the PMMA/PS interface in the vicinity of the 3-phase contact line can be characterized by the height *h*, i.e. peak to baseline distance. Shown in Figure 9 is the height of the deformation of the primary cylinder at the PMMA/PS interface under the PS columns as a function of the ratio of PS and PMMA molecular weights. As seen, as this ratio increase or as the mobility of PMMA increases in comparison to that of PS, the extent of deformation at the PMMA/PS interface increases. In addition, for a given ratio of molecular weights, as the applied field strength increases by increasing the applied voltage while fixing the separation distance, *d*, between two electrode, or by decreasing *d* while keeping the applied voltage (inset in
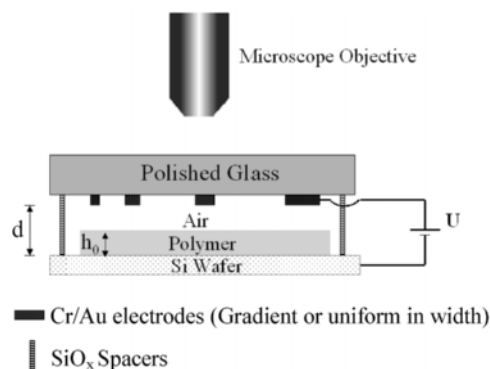
Figure 10. Sketch of the sample configuration in the study. Either periodic or gradient Au/Cr electrodes with finite width in *y* can be prepared by electric beam lithography.
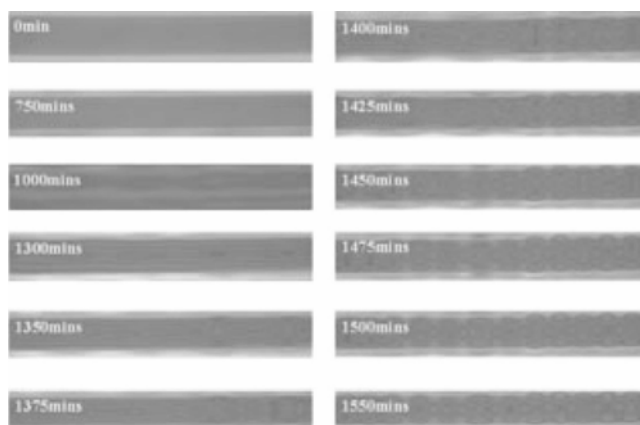

Figure 11. Spatio-temporal evolution of 340 nm PI thin film under 50 μm Au/Cr stripe with 15 V applied.

Figure 9), the magnitude of the deformation increases.

Rather than sandwiching the polymer thin film in between two infinite long electrodes, patterned electrodescan be used that introduce a local enhancement of the applied field. The evolution of surface instabilities under finite size upper electrode leading to the pattern formation and selection in the electric field is being investigated. Figure 10 shows the experimental configuration in the study. The stripe-like Cr/Au electrodes are infinitely long in *x*, but with a finite width in *y*. A real time study of 340 nm PI thin film under 50 μm Au/Cr electrode with 15 V applied is shown in Figure 11. The buildup of instability is clearly evident around 1000 mins. With time, the amplitudes of fluctuations are enhanced, the formation of PI columns, which bridge between two electrodes, can be seen in 1350 mins. As time progresses, more columns

are formed and the characteristic wavelength of 40 um with an average diameter of 17 um is established eventually. Experiments are being performed as a function of the film thickness, the applied field, the width and the shape of the pattern electrodes to quantify the confinement effect imposed by the finite size upper electrode.

Acknowledgments

References

1. L. Larrondo and R. J. St. John Manley, *J. Polym. Sci.*, *Polym. Phys.*, **19**, 909, 921, 933 (1981).
2. J. Doshi and D. H. Reneker, *Electrostatics*, **35**, 151 (1995).
3. D. H. Reneker and I. Chun, *Nanotechnology*, **7**, 216 (1996).
4. M. M. Hohman, M. Shin, G. C. Rutledge, and M. P. Brenner, *Phys. Fluids*, **13**, 2201, 2221 (2001).
5. J. R. Melcher, *Phys. Fluids*, **4**, 1348 (1961).
6. G. I. Taylor and A. D. McEwan, *J. Fluid Mech.*, **22**, 1 (1965).
7. M. Reynolds, *Phys. Fluids*, **8**, 161 (1965).
8. J. R. Melcher and C. V. Smith, *Phys. Fluids*, **12**, 778 (1969).
9. J. A. Saville and O. Vizika, *J. Fluid Mech.*, **239**, 1 (1992).
10. D. A. Saville, *Colloids Surf. A.*, **92**, 29 (1994).
11. D. A. Saville, *Annu. Rev. Fluid Mech.*, **29**, 27 (1997).
12. E. Schäffer, T. Thurn-Albrecht, T. P. Russell, and U. Steiner, *Nature*, **403**, 874 (2000).
13. E. Schäffer, T. Thurn-Albrecht, T. P. Russell, and U. Steiner, *Europhys. Lett.*, **53**, 518 (2001).
14. Z. Lin, T. Kerle, S. M. Baker, D. A. Hoagland, E. Schäffer, U. Steiner, and T. P. Russell, *J. Chem. Phys.*, **114**, 2377 (2001).
15. Z. Lin, T. Kerle, T. P. Russell, E. Schäffer, and U. Steiner, *Macromolecules*, **35**, 3971 (2002).
16. Z. Lin, T. Kerle, T. P. Russell, E. Schäffer, and U. Steiner, *Macromolecules*, **35**, 6255 (2002).
17. P. Lambooy, K. C. P helan, O. Haugg, and G. Krausch, *Phys. Rev. Lett.*, **76**, 1111 (1996).